Nano Research 2016, 9(5): 1346–1357
DOI 10.1007/s12274-016-1030-0
Research Article
ISSN 1998-0124
CN 11-5974/O4

Ultrasensitive strain gauge with tunable temperature coefficient of resistivity

Lizhi Yi[1], Weihong Jiao[1], Changming Zhu[1], Ke Wu[1], Chao Zhang[1,2], Lihua Qian[1,2] (✉), Shuai Wang[3], Yingtao Jiang[4], and Songliu Yuan[1] (✉)

[1] *School of Physics, Huazhong University of Science and Technology, Wuhan 430074, China*
[2] *Flexible Electronics Research Center, Huazhong University of Science and Technology, Wuhan 430074, China*
[3] *School of Chemistry and Chemical Engineering, Huazhong University of Science and Technology, Wuhan 430074, China*
[4] *Nevada Nanotechnology Center & Department of Electrical and Computer Engineering, University of Nevada, Las Vegas, Nevada 89154-4026, USA*

Received: 6 November 2015
Revised: 7 January 2016
Accepted: 25 January 2016

KEYWORDS
strain gauge,
flexible gauge,
Au nanoparticle,
sound-wave detection,
radial-artery detection,
electron tunneling

ABSTRACT

We demonstrate an ultrasensitive strain gauge based on a discontinuous metal film with a record detection limit as low as 8.3×10^{-6}. Constructed by well-tunable crevices on the nanometer scale within the film, this gauge exhibits an ultrafast dynamic response to vibrations with a frequency range of 1 Hz to 10 kHz. More importantly, the temperature coefficient of resistivity (TCR) of the metal film is tunable owing to the cancellation effect caused by the possibility of tunneling across the nanoscale crevices (showing a negative temperature dependence) and the electron conduction within the metal islands (showing a positive temperature dependence). Consequently, a nullified TCR is achievable when the crevice size can be precisely controlled. Thus, a fabrication strategy to precisely control the nanoscale crevices was developed in this study through the real-time tracking of the electrical conductivity during thermal evaporation. The ultrasensitive strain gauge with a tunable thermal drift introduces numerous opportunities for precision devices and wearable electronics with superior reliability.

1 Introduction

The electrical resistivity of metal nanoparticles (NPs) and their derivatives with various geometries and morphologies is a fundamental parameter for enabling the application of NPs in optical or optoelectronic devices [1], non-volatile memory [2], flexible strain sensors [3], and wearable electronics [4]. Recent investigations of strain gauges based on well-defined NP arrays revealed fascinating characteristics, including an excellent sensitivity, ultrafast dynamics in response to strain, and a reliable output electrical signal [5], especially for single-layer metal NPs developed by self-assembly [6] and physical vapor deposition [7], both of which are versatile methods for creating homogeneous infrastructures. Excellent sensitivity results

Address correspondence to Lihua Qian, lhqian@mail.hust.edu.cn; Songliu Yuan, yuansl@hust.edu.cn

from the small crevices between neighboring NPs, which can be precisely tailored on the nanometer scale, and the relative change in the electrical resistance follows an exponential relationship with respect to the size of the nanoscale crevices. The lowest strain to be detected can approach 9.4×10^{-5} in a single layer of Au NPs [8], which is more sensitive than the flexible strain gauges reported in the literature [9]. Furthermore, the ultrafast dynamics in response to an external stimulus intrinsically stem from the timely evolution of nanoscale crevices. Compared with other flexible nanostructures, such as graphene [10], nanotubes [11] and nanowires [12], the electrical contacts tend to change simultaneously in response to the external loading and unloading, so that no obvious hysteresis in the electrical signal is observed even if the loading/unloading rate is as high as 500 Hz [5]. This feature suggests the potential to detect acoustic vibrations with an infinitesimal amplitude, which extends the application of NPs arrays toward precision devices with ultrafast dynamics [5]. Finally, the conductive path within NP arrays or their derivatives can be automatically formed in two-dimensional (2D) or three-dimensional (3D) networks [13]. Therefore, the prodigious reliabilities of the output signals are experimentally manifested in a single layer of NP and 3D NP ensembles.

Although the aforementioned promising advantages make NP ensembles flexible gauges with ultrafast dynamics for the reliable detection of acoustic vibration, the applications of NP ensembles can be advanced considerably, especially by eliminating the irregular drift in the background current and promoting the detection limit that is demonstrated in some 2D infrastructures, such as metal films containing parallel crevices [14], vertically arranged nanowires [15], and ultrathin graphene networks [16]. Usually, the internal resistance of the active unit varies with respect to the environment temperature, which induces a random disturbance of the electrical signal in the case of a large temperature coefficient of resistivity (TCR) during the electrical characterizations. Therefore, suppressing the thermal drift of the active units may be an effective method for improving the signal-to-noise ratio (SNR). On the other hand, in our previous investigation, a flexible gauge made of nanoscale crevices within an NP monolayer assembled onto a flexible polymer was demonstrated, and this device, with a gauge factor (defined as the relative change in the electrical signal divided by the strain) as high as 300, reliably detected mechanical vibrations at a frequency as high as 20 kHz [5]. However, one drawback of this device is that a reliable output signal can be attained only when the vibration amplitude—a reflection of the mechanical strain—is amplified by an exciter. A natural extension of that work is to further improve the dynamic performance with respect to both the detection sensitivity and background noise in the presence of low-amplitude vibrations.

Herein, a strategy to increase the controllability of the nanoscale crevices by the real-time tracking of the electrical conductivity during thermal evaporation is described. We show that the detection limit of the mechanical strain reaches 8.3×10^{-6}, which is more than one order of magnitude lower than the best results reported in the literature. This new and much-improved strain gauge, with its TCR of nearly zero and high sensitivity, lends itself well to various important applications, such as non-contact acoustic-wave detection and the real-time monitoring of physiological parameters.

2 Experimental

2.1 *In situ* monitoring of electrical current flowing through strain gauge

During the deposition of an ultrathin Au film, the resistance of the active unit was detected *in situ* by a Keithley 6487 picoammeter. Two metal wires connected the electrodes of the gauge to the picoammeter outside of the vacuum chamber during the thermal evaporation. A bias voltage of 0.2 V was applied to the active unit, and the current flowing through the gauge was detected by the picoammeter in real time and recorded by a data acquisition card (DAC, National Instruments).

2.2 Supply of mechanical vibrations with different frequencies

In vibration-frequency tests, the strain gauge was laid horizontally during the measurement. One terminal

was immobilized, and the other terminal was operated by a vibration executor driven by a function generator tunable over the frequency range of 1–20,000 Hz. For tests in the low-frequency range, in the case of the droplet-induced vibration, the gauge functioned as a cantilever, with one terminal sitting horizontally on a static stage and the other in a suspended state. For testing the acoustic vibration, both the terminals of the gauge were immobilized, and the air vibration caused when human participants spoke was employed.

2.3 Real-time measurement of mechanoelectrical characterization

The strain gauge was connected to a resistor in parallel. A stable bias voltage was applied to the gauge. During the bending or vibration of the strain gauge, the voltage between the two terminals of the resistor changed because of the change in the active unit resistance, which was recorded by the DAC.

2.4 Measurement of TCR

A four-probe method was utilized to measure the resistance of the active unit. For electrical measurements below room temperature, the resistance was detected by using a physical-property measurement system, which can maintain a low-temperature environment in the range of 4 to 300 K. For electrical measurements at room temperature, the gauge was placed in a furnace. The resistance and exact temperature were simultaneously recorded by the DAC.

3 Results and discussion

3.1 Gauge fabrication

The active units of the strain gauge and Au electrodes were created by a two-step lithography process, as illustrated in Fig. 1. A polyethylene terephthalate (PET) film with dimensions of 60 mm × 15 mm × 0.1 mm was selected as the primary substrate to support the active unit and the electrodes. PET was selected as the substrate primarily according to two considerations. First, it can withstand the temperature increase that occurs when the conductive electrodes are fabricated by thermal evaporation. Second, it is flexible and difficult to stretch, which is beneficial for applying a small strain. A wire with a diameter of 90 μm placed on to the PET film was utilized as a mask during the first stencil-lithography step (Fig. 1(a)). Au films deposited on the exposed surface were employed as two electrodes separated by the mask. The Au electrodes were sufficiently thick (>30 nm) to guarantee their negligible resistance (less than 1 Ω) compared with the individual active unit of the strain gauge (0.005–16 MΩ). After the mask was removed, a blank slit 90 μm in width remained for the creation of an active unit (Fig. 1(b)). The second mask, with a rectangular window, intersected with the slit (Fig. 1(c)), ensuring that its longitudinal axis connected the two isolated electrodes. The window width varied from 0.1–1 mm to satisfy the measurement range of the instrument as needed in the characterization of the electrical resistance. After the secondary evaporation, the Au film across the two electrodes appeared as a bright strip (Fig. 1(d)) with a distinct contrast, as indicated by the scanning electron microscopy (SEM) image shown in Fig. 1(e). The rectangular segment confined within the two electrodes was actually the active unit of the strain gauge. During the device fabrication, its electrical resistance can be monitored *in situ* to optimize the device structure precisely. In this study, the strain gauge was directly fabricated on the PET substrate, without an adhesion layer such as Cr, because most Au thin films are several nanometers thick, and the deposition of an adhesion layer affects the electron transport between neighboring junctions.

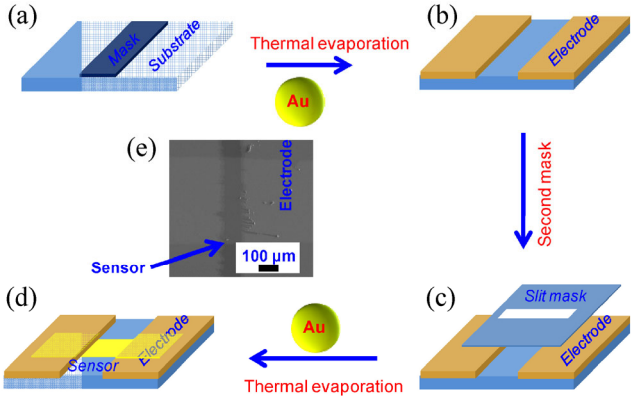

Figure 1 Schematic of the device fabrication. (a)–(d) Experimental procedure to fabricate the electrodes and the active units of the strain gauge. (e) SEM photograph of the gauge, where the grey strip across the channel is the active unit.

The electrical current flowing through the active unit depended on the film thickness, as indicated by Fig. 2(a), when a voltage of 0.2 V was applied (planar area of the active unit was approximately 90 μm × 450 μm). Initially, the electrical current gradually increased from 0 to 1 μA when the thickness of active unit was less than 5 nm. A steep surge occurred when the film thickness approached 7 nm. In this case, the electrical current increased monotonically, with a nearly constant slope of 1 μA/Å. Figure 2(b) shows a transmission electron microscopy (TEM) photograph of the sample labeled No. 2 in Fig. 2(a); here, we observe that all the isolated islands had irregular geometries, and most of them were nearly circular or spindle. All the crevices between the neighboring islands ranged from 1–5 nm in size, and most of them were as small as 3 nm, as shown in the inset of Fig. 2(b). For samples No. 3, No. 4, and No. 5, random aggregations between neighboring islands occurred (Fig. S1 in the Electronic Supplementary Material (ESM)). For sample No. 6, a continuous film with a few nanoscale voids was observed. The procedure to fabricate active units can be applied for other metals, including Ag and Cu, by checking the current-thickness relationship shown in Fig. S2 (in the ESM). In this study, Au film was selected for the active unit because of its chemical inertness in the ambient environment.

To unveil the quantitative relationship between the film thickness and the sensing performance, all six samples labeled in Fig. 2(a) were configured as strain gauges in order to examine their response as a function of the strain. The gauges were utilized to cover cylinders with different diameters for obtaining accurate strain values. The curves corresponding to the six samples are presented in Fig. S1 (in the ESM). To test the detection limits, the gauges were vertically stalled in order to measure the mechanical strain accurately during the bending of the PET film. One

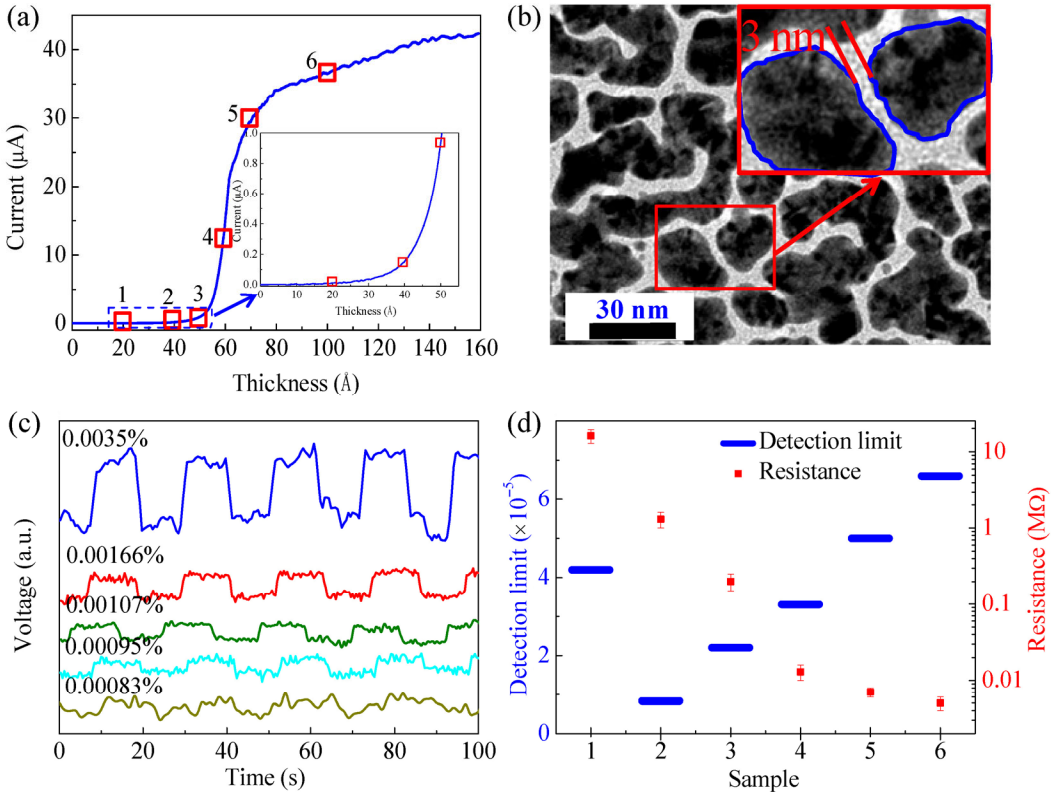

Figure 2 Electrical properties and detection limit of various strain gauges. (a) The electrical current flowing through the active unit varied with the thickness of the active unit when a bias voltage of 0.2V was supplied. The labeling numbers define the parameters used in this work to fabricate the six gauges. (b) TEM photograph of the active unit in gauge No. 2. (c) Temporal change in the electrical voltage when the distinct levels of strain were loaded and unloaded onto gauge No. 2. (d) Detection limits and electrical resistances of all six gauges investigated in this work.

terminal of the gauge was immobilized, and the other terminal was motorized by a translation stage. With this geometrical configuration, the mechanical strain can theoretically be precisely estimated, and the detailed methodology is presented in the ESM. As an example, the electrical resistance of the gauge (sample No. 2) when mechanical strains at different levels were periodically applied and released is presented in Fig. 2(c). Reproducible pulses of the electrical current appeared when the gauge was repeatedly bent, demonstrating the robustness and reliability of the device. These results are similar to observations of an NP monolayer assembled onto a PET film [6]. To further examine the reliability and durability of the gauge, a long-term cycling test was conducted, and its results are included in the ESM. Importantly, when the pulse strain decreased from 1.66×10^{-5} to 8.3×10^{-6}, the change in electrical resistance remained visible, in which case the SNR was ~1.98 for a strain level of 0.00083%, demonstrating the ultrasensitive capability of the device. This detection limit of 8.3×10^{-6} is 10–100 times better than that of previously reported metal NPs [9]. In this case, the gauge factor can be as high as 350, which is analogous to flexible gauges based on NP networks or arrays fabricated by different methods [17]. This sensitivity is far better those that of previously reported metal oxides, carbon-incorporated materials, and 3D nanostructures [18]. A detailed explanation of the proposed mechanism is provided in the following section. Figure S1 in the ESM shows the other five gauges, which had a slightly poorer sensitivity. Figure 2(d) shows the detection limit and the electrical resistance of all six gauges assembled in this work. Unless it is explicitly stated otherwise, all the device characterizations in the following section were collected for sample No. 2.

3.2 Sensing performances

As previously mentioned, the NP monolayer with the well-defined crevices had a superior sensitivity, making it suitable for the construction of precision devices. To identify its robustness and high sensitivity, the gauge was used to detect mechanical vibrations at low frequencies. First, the PET strip functioned as a cantilever, whose vibration characteristics are well described in theory. The strain gauge placed on the strip monitors the oscillating vibration in real time. To demonstrate this capability, one terminal of the strip horizontally was attached to a fixed stage, as shown in Fig. 3(a), while the other terminal was in a suspended state. Acetone droplets released from various altitudes created an initial disturbance to the free terminal, triggering a periodic oscillation at a certain frequency. Figure 3(b) shows the typical electrical waveform output from a strain gauge when one 40 μL acetone droplet (~30 mg) was released from an altitude of 40 mm. Prior to the droplet-induced disturbance, the voltage was 7.342 V. At the moment of the droplet release, the voltage almost immediately decreased to 7.336 V because of the primary strain exerted onto the gauge after the bending of the strip cantilever (see Fig. 3(b)). The net change of the output voltage reveals that the instantaneous strain exerted onto the gauge was ~7.4×10^{-5}. After the droplet hit the device, the strip cantilever behaved like a damping vibrator in the air, with a constant frequency and attenuated amplitude. Theoretically, the envelope of the voltage waveform decreases exponentially with the damping time. Assuming a linear relationship between the output voltage and the vibrating amplitude, the vibration profile can be fitted by the equation of $y = 0.015 \times \exp(-0.98t)$, which indicates that the substrate was under-damped. The amplitude of this damping vibrator was reliably tracked for 9 s, until the oscillating signal faded completely (see Fig. 3(c)). According to the magnitude of the output voltage at the end of the 9 s, the minimum change in the vertical coordinate was ~100 μm (corresponding to a strain of ~7×10^{-6}), confirming the ultrasensitive nature of the developed gauge. More importantly, the initial voltage was restored after the complete evaporation of the acetone droplet in 80 s, demonstrating the robustness and reliability of the gauge.

When acetone droplets with the same volume were released at various altitudes, e.g., 5, 10, 20, 30, and 40 mm, the vibration amplitude of the cantilever increased with the altitude (see Fig. S3(a)). Interestingly, the equilibrium voltage during the oscillating vibration remained constant (see Fig. 3(d)) even if the attitude of the released acetone droplet varied. The resonant frequency of the cantilever under different experimental settings was fixed at 8.9 Hz (Fig. 3(d)) because

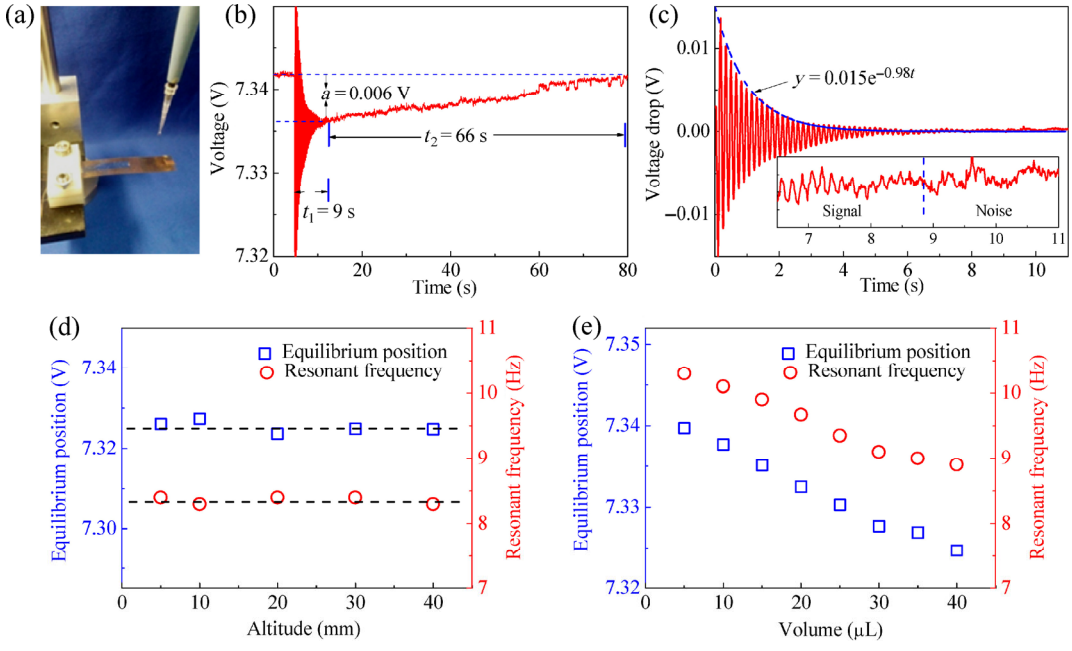

Figure 3 Electrical responses of the strain gauge to the disturbance of the acetone droplets. (a) Photograph of the acetone droplet hitting the surface of the gauge. (b) Temporal change in the electrical voltage of the gauge at different stages of the droplet disturbance, including dropping, vibration, and drying. (c) Voltage as a function of time during the vibration process, where the blue dotted line shows the fitting curve of the vibration waveform envelope. (d) The frequency/equilibrium position of the gauge varied with respect to the altitude of the acetone droplet released. (e) The frequency/equilibrium position of the gauge varied with respect to the volume of the acetone droplet released.

the inherent vibration frequency and the equilibrium position were only related to the mass distribution of the cantilever, and when droplets with the same volume were released at different altitudes, the mass distribution does not change. The equilibrium voltage and vibration frequency confirm that the output electrical signal truly reflects the intrinsic characteristics of the PET strip during the mechanical vibration. In another test, acetone droplets with different volumes in the range of 5–40 μL were released from the same altitude. The electrical waveforms obtained from the gauge in both cases are very similar, except for differences in the amplitude and equilibrium voltage, which depend on the mass of the acetone droplets (see Fig. S3(b) in the ESM). In these experiments, the vibration frequency increased from 8.9 to 10.3 Hz (Fig. 3(e)) when the acetone volume decreased from 40 to 5 μL. Thus, altering the mass of the acetone droplet changed the intrinsic mass of the cantilever, implying changes in the resonant frequency and equilibrium voltage (Fig. 3(e)). Generally, the electrical waveforms, which were analyzed in both the time and frequency domains, reveal the excellent reliability and superior sensitivity of the gauge, suggesting its usefulness for the detection of low-frequency and small-amplitude mechanical vibrations. To exploit these characteristics, both the strain gauge and the measurement module kits were integrated into a packaging box as one functional device. The entire device can be mounted onto a fence and employed as an intrusion-prevention system. Details are included in the Fig. S4 and Movie S1 in the ESM.

In addition to detecting vibrations as a cantilever, the gauge can be used to monitor the blood-pressure waveforms of human radial arteries in real time. The gauge is promising compared with the different nanostructures used in several previous investigations [4, 14, 15, 19, 20]. The detailed parameters of the gauge are presented in Table S1 (in the ESM). In this study, the gauge was wrapped around the wrist of a participant (see Fig. 4(a)), and the periodical motion of the radial artery of the participant stimulated a pulse

strain of electrical voltage when a constant voltage was applied. The wrist pulses were tracked accurately in the normal condition (80 pulses/min) and after physical exercise (105 pulses/min), as shown in Fig. 4(b). A typical radial-artery pulse waveform was obtained with two clearly distinguishable peaks (P_1 and P_3) and a systolic augmentation shoulder (P_2) (Fig. 4(c)). This type of profile results from the contraction of the blood pressure from the left ventricle and the reflective wave from the lower body [4, 21]. The radial-augmentation index $A = P_2/P_1$ is a characteristic parameter for arterial stiffness and is related to the age of the subject [15, 22], The frequencies of the pulses under the two conditions differed slightly. For a series of waveforms measured using our gauge, the average value of A was estimated as 0.7, suggesting that the data were collected from a healthy 23-year-old man [4, 15]. These results demonstrate that subtle differences in blood pulses can be recorded by using this gauge, indicating its potential application as a wearable diagnostic device to monitor the physiological conditions of humans in real time.

In this work, the strain gauge made of one layer of Au NPs enabled us to detect mechanical vibrations in the high-frequency region. To verify the dynamic response performance, a vibration exciter controlled by a function generator exerted a mechanical strain with a desired frequency to the gauge. When mechanical stimuli with a broad range of frequencies were applied, the resulting temporal waveforms (see Figs. S5(a) and S5(b) in the ESM) confirmed the reliability of the output signal in the frequency range of 10–10,000 Hz. To qualitatively test the performance under acoustic vibrations, the gauge was exposed to laryngeal vibrations without amplitude amplification by the exciter when a person read the word "Hello" (see Fig. 5(a)). Figure 5(b) shows the waveform of the electrical signal detected by the gauge. The experimental data collected by the gauge were transformed into audio files and are provided in Audios S1–S3 (in the ESM). In Fig. 5(c), which shows the frequency-domain waveform of the laryngeal vibration, we observe that the resonance frequency of the vibration was ~260 Hz.

The gauge can detect vibrations in not only the contact mode but also the non-contact mode, as shown in Fig. 5(d). For testing this, a person spoke a word into a microphone integrated with our gauge and electrical circuit. Figure 5(d) shows the program interface, wherein the waveforms were displayed on the computer screen in real time when the person spoke. Figure 5(e) presents time-domain waveforms of the electrical signals for three different people speaking the word "Hello" (refer to Audios S4–S6 in the ESM), and the frequency-domain analysis shown in Fig. 5(f) indicates that these persons had quite different timbres. The resonant frequency of the second person (the blue line in Fig. 5(f)) was far higher than that of the others. Interestingly, the vibration frequencies detected for the laryngeal and the non-contact modes differ. This discrepancy is related to the different media (muscles and air) in which the vocal-cord vibrations propagated. In the contact mode, the vibration passed through the bones and muscles, and the vibration frequency was reduced by the nonlinear damping of the bones and muscles.

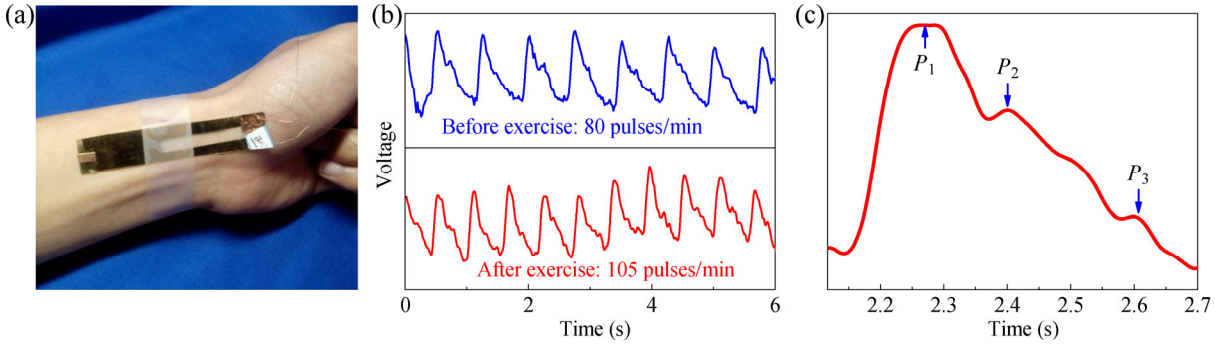

Figure 4 Reliable detection of radial-artery pulses. (a) Strain gauge mounted onto the radial artery of a participant. (b) Electrical waveform of the strain gauge in response to radial-artery pulses. (c) Typical pulse waveform of a single radial-artery pulse.

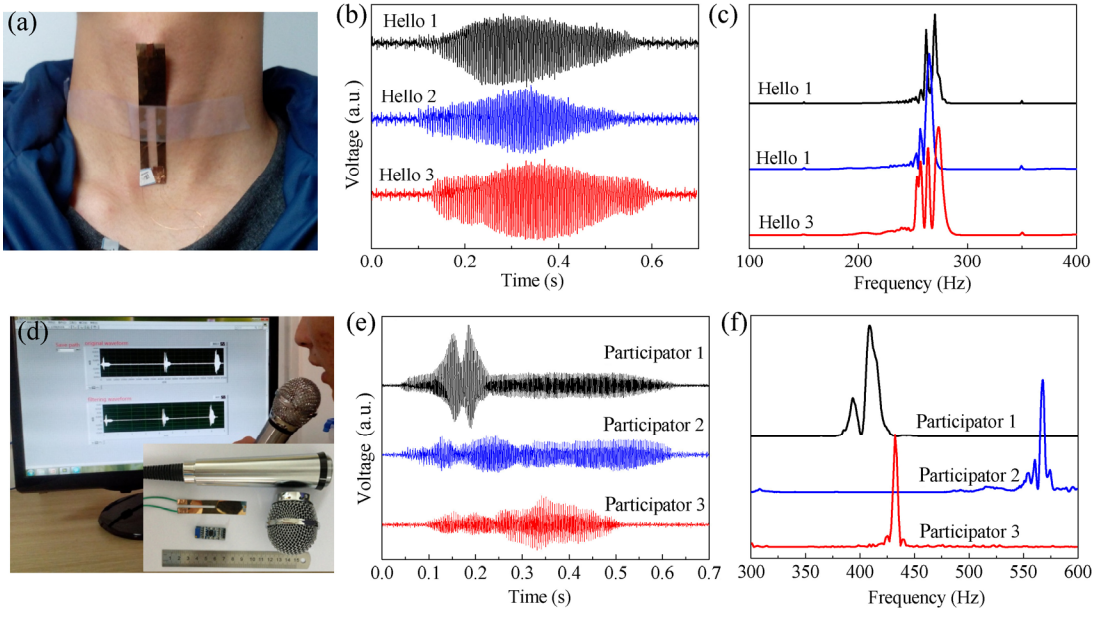

Figure 5 Ultrafast dynamics of the strain gauge. (a) Photograph showing the ultrasensitive strain gauge placed onto the larynx of a participant for operation as a vibration detector. (b) Electrical waveforms of the strain gauge in response to a person saying the word "Hello". (c) Frequency analysis of the waveforms shown in (b). (d) Photograph showing the interface when the strain gauge functioned as a microphone. The inset shows the components of the device. (e) and (f) Time- and frequency-domain representations of the waveforms obtained from three persons saying "Hello".

3.3 Tunable TCR

To understand the sensing mechanism of the developed strain gauge, the microstructure of the ultrathin Au film should be examined. This film, with a thickness of several nanometers, consists of an array of isolated islands, and most of the crevice gaps are a few nanometers in size, as shown in Fig. 2(b). In this work, the active units of the strain gauge are considered as composite materials including the isolated islands separated by the air junctions. Therefore, the total resistance of the composites is described as

$$R = (R_j + R_i)\cdot N \quad (1)$$

where R_j is the resistance of the junction, R_i is the resistance of the Au island, and $N = L/(r + d)$ is the number of junctions along the potential dropping during the electrical measurement. Here, L is the length of the gauge element, r is the average diameter of the Au islands, and d is the average gap size.

In the junction, the electrical resistance is correlated with electrons tunneling from one isolated island to its neighbors. According to electron tunneling theory, the electrical resistance at the junction is described as [23]

$$R_j = \frac{V}{AJ} = \frac{h^2 d}{Ae^2\sqrt{2m\varphi}}\exp\left(\frac{4\pi d}{h}\sqrt{2m\varphi}\right) \quad (2)$$

where A is the cross sectional area of the islands, h is Planck's constant, e is the electron charge, m is electron mass, and φ is the barrier height of the junction.

On one island, the resistance depends on the geometrical parameters and thus can be described as

$$R_i = \rho r / A$$

Here, ρ is the resistivity of the Au film, and r is the island size. Considering the temperature effect, Eq. (1) becomes

$$R = (R_j f_j(T) + R_i f_i(T))\cdot N \quad (3)$$

Here, $f_j(T)$ and $f_i(T)$ are coefficients related to the temperatures of the junction and the island, respectively. Note that $f_j(T)$ has the following form [24]

$$f_j(T) \propto \exp\left(\frac{e^2/d}{kT}\right) \quad (4)$$

Here, k is the Boltzmann constant. Clearly, $f_j(T)$ decreases as the temperature increases, indicating that R_j has a negative TCR. In this condition, the electron tunneling can be thermally activated. At a higher temperature, more activated electrons participate in the electron transport. Consequently, the resistance within the junction decreases as temperature rises. Within an island, the resistance results from the lattice scattering of electrons. In this case, $f_i(T)$ can be described as

$$f_i(T) \propto T^{\alpha} \quad (1 < \alpha < 5) \tag{5}$$

Equation (5) indicates that the metallic film has a positive TCR. Figure 6(a) shows the temperature dependence of the $\Delta R/R_{260K}$ for two typical gauges below room temperature. The samples 4 and 9 nm thick had a negative and positive TCR, respectively. Clearly, the Au film with a thickness of 4 nm comprised individual islands (Fig. S1(b) in the ESM), and the resistance significantly depended on the tunneling barrier of the thermally activated electrons within the junction. The Au film with a thickness of 9 nm exhibited metallic behavior, and the resistance mainly depended on the lattice scattering of the free electrons within the islands.

As previously described, the electron transport within the inter-particle junction and the isolated island exhibited opposite signs in their TCRs. The actual TCR of the active unit thus depends on the net effect of these two distinct mechanisms in electron transport. This indicates that the TCR can be adjusted by controlling the film thickness. We checked the TCR of the gauges above room temperature because most strain gauges are utilized around room temperature. Figure 6(b) shows the temperature dependence of the $\Delta R/R_{310K}$ for two typical gauges near room temperature. As illustrated in Fig. 6(b), the TCR changed from negative (–0.0031/K) to positive (+0.0014/K) when the thickness of the Au film increased from 5 to 6 nm. The TCR of the Au film with a thickness of 5.5 nm was

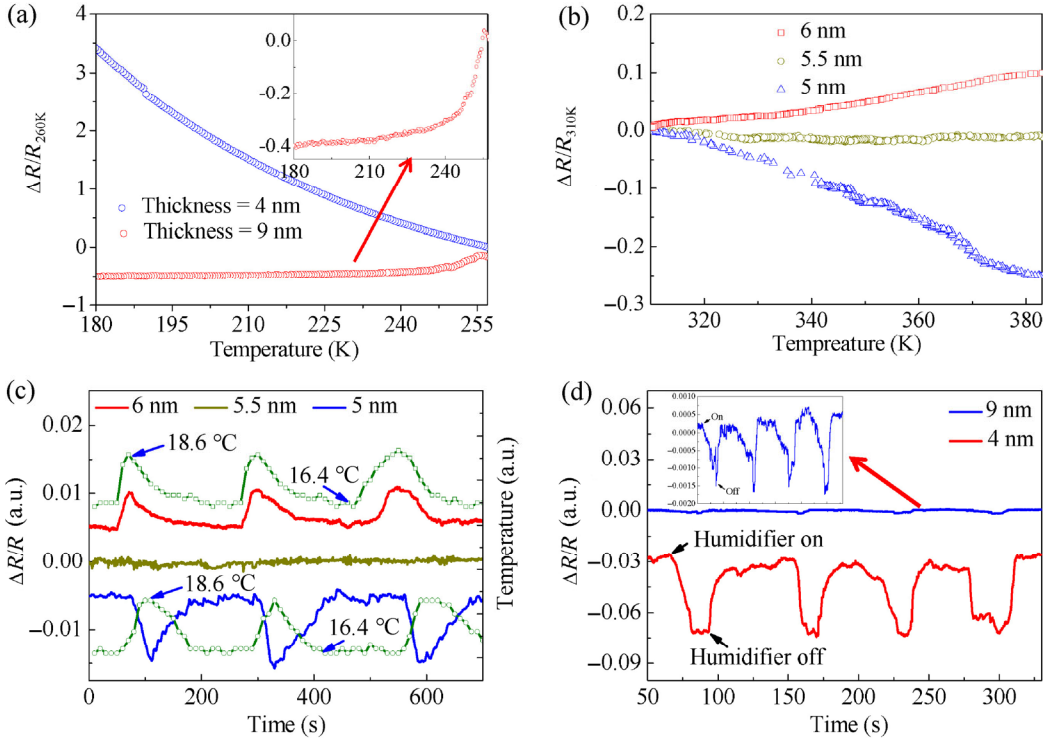

Figure 6 Effect of the temperature on the electrical resistance. (a) Relative change in the electrical resistance $\Delta R/R_{260K}$ below room temperature. (b) Relative change in the electrical resistance $\Delta R/R_{310K}$ above room temperature. (c) Responses of the gauge to an abrupt temperature change in the environment. The red and blue curves were vertically shifted for visual guidance. (d) Responses of the gauge to changes in the humidity of the environment. The red and blue curves show the temporal dependence of $\Delta R/R$ when the humidifier was powered on and off, respectively.

zero, which offers a method to design ultrasensitive strain gauges with negligible thermal drift. To verify the advantage of a TCR of zero, a minor temperature fluctuation was artificially introduced in order to check the drift in the background current. As shown in Fig. 6(c), the resistance of the gauge with a thickness of 6 nm increased by 0.5% when the environment temperature increased from 16.4 to 18.6 ˚C, whereas that of the gauge with a thickness of 5 nm exhibited an opposite trend, decreasing by 1.0% over the same temperature range. Clearly, a TCR of zero offers an avenue to design piezoresistive gauges for applications in precision devices, e.g., an ultrasensitive and reliable gauge with a negligible TCR for strain sensing.

In addition to examining the effect of the temperature, we tested the response of the gauge to humidity. The strain gauge, a humidifier, and a hygrometer with a resolution of 1% were integrated in a box. The humidity in the box was tailored by the humidifier, and the resistance of the strain gauge was simultaneously tested. Our sensor enabled responding to the ambient humidity to some extent when the humidifier was powered on or off. An electrical resistance with a magnitude of 8% was output from the sensor when the humidity changed by ~2% (Fig. 6(d)).

3.4 Strategies to design ultrasensitive strain gauge

The sensitivity is one of the most crucial parameters in a strain gauge [25, 26], especially for precision devices. The piezoresistive strain gauge based on the NP monolayer exhibited an exponential relationship between the relative change in the electrical resistance and the size of the nanoscale crevices [27, 28], which intrinsically gives it a superior sensitivity compared with some carbon-incorporated nanostructures or composite nanostructures with 2D/3D stacking [29]. The sensitivity of the NP ensembles reported in the literature is insufficient for the detection of small-amplitude mechanical vibrations, which may stem from the nonhomogeneous distribution of the nanoscale crevices and the efficient acquisition of the electrical signal [9]. The significantly enhanced sensitivity of our gauge is ascribed to the gap size being well-controlled, as shown in Fig. 2(b), while the electron transport of the NP monolayer was monitored *in situ* during thermal evaporation. An extrinsic way to improve the detection sensitivity is to optimize the measurement circuit and the ambient environment during the data collection in order to enhance the SNR. In this study, the TCR was tunable across the zero, implying that the detailed structures of the NP monolayer can be further optimized in upcoming investigations. This strategy introduces an avenue to rationally refine the geometrical parameters of the isolated islands, such as the crevice gap size and the shape and compositions of the deposited NPs, in which case the simultaneous attainment of a superior sensitivity and TCR of zero may be achieved. Thus, the effect of the ambient temperature on the electrical resistance will be eliminated to a great extent, which is significant for collecting electrical signals with an extremely low level. In principle, this design strategy for a superior sensitivity is applicable for strain gauges made of other materials and nanostructures [30–32].

4 Conclusions

In this study, 2D NP arrays deposited onto a flexible polymer were configured as strain gauges. The detection limit became as low as 8.3×10^{-6}, which is 10–100 times better than that of NP-based strain gauges reported in the literature. The high sensitivity is attributed to the significant effect of the electrical resistance on the crevice gap between the neighboring NPs. Similarly to strain sensors based on nonmetallic nanostructures, our gauge has a tunable TCR. The negative or positive values of our gauge were due to the net effects of the electron tunneling between the neighboring particles and the lattice scattering of electrons, which depend on the detailed microstructure of metal film. Therefore, a TCR of zero can be obtained by selecting the appropriate thickness, which introduces a method for fabricating ultrasensitive strain gauges without thermal drift for various applications in precision devices.

Acknowledgements

This work was partially supported by Innovation Funding of HUST for International Collaborations

(No. 2014ZZGH018), Specialized Research Fund for the Doctoral Program of Higher Education (No. 20130142120089), and National Natural Science Foundation of China (Nos. 51371084 and 91545131).

Electronic Supplementary Material: Supplementary materials (the supporting figures, tables, audio and movie files) is available in the online version of this article at http://dx.doi.org/10.1007/s12274-016-1030-0.

References

[1] Shen, S. X.; Meng, L. Y.; Zhang, Y. J.; Han, J. B.; Ma, Z. W.; Hu, S.; He, Y. H.; Li, J. F.; Ren, B.; Shih, T. M. et al. Plasmon-enhanced second-harmonic generation nanorulers with ultrahigh sensitivities. *Nano Lett.* **2015**, *15*, 6716–6721.

[2] Talapin, D. V.; Lee, J. S.; Kovalenko, M. V.; Shevchenko, E. V. Prospects of colloidal nanocrystals for electronic and optoelectronic applications. *Chem. Rev.* **2010**, *110*, 389–458.

[3] Rogers, J. A.; Someya, T.; Huang, Y. Materials and mechanics for stretchable electronics. *Science* **2010**, *327*, 1603–1607.

[4] Gong, S.; Schwalb, W.; Wang, Y. W.; Chen, Y.; Tang, Y.; Si, J.; Shirinzadeh, B.; Cheng, W. L. A wearable and highly sensitive pressure sensor with ultrathin gold nanowires. *Nat. Commun.* **2014**, *5*, 3132.

[5] Yi, L. Z.; Jiao, W. H.; Wu, K.; Qian, L. H.; Yu, X. X.; Xia, Q.; Mao, K. M.; Yuan, S. L.; Wang, S.; Jiang, Y. T. Nanoparticle monolayer-based flexible strain gauge with ultrafast dynamic response for acoustic vibration detection. *Nano Res.* **2015**, *8*, 2978–2987.

[6] Zhang, C.; Li, J.; Yang, S. S.; Jiao, W. H.; Xiao, S.; Zou, M. Q.; Yuan, S. L.; Xiao, F.; Wang, S.; Qian, L. H. Closely packed nanoparticle monolayer as a strain gauge fabricated by convective assembly at a confined angle. *Nano Res.* **2014**, *7*, 824–834.

[7] Zheng, M. Y.; Li, W. Y.; Xu, M. J.; Xu, N.; Chen, P.; Han, M.; Xie, B. Strain sensors based on chromium nanoparticle arrays. *Nanoscale* **2014**, *6*, 3930–3933.

[8] Jiao, W. H.; Yi, L. Z.; Zhang, C.; Wu, K.; Li, J.; Qian, L. H.; Wang, S.; Jiang, Y. T.; Das, B.; Yuan, S. L. Electrical conduction of nanoparticle monolayer for accurate tracking of mechanical stimulus in finger touch sensing. *Nanoscale* **2014**, *6*, 13809–13816.

[9] Segev-Bar, M.; Haick, H. Flexible sensors based on nanoparticles. *ACS Nano* **2013**, *7*, 8366–8378.

[10] Chen, Z. P.; Ren, W. C.; Gao, L. B.; Liu, B. L.; Pei, S. F.; Cheng, H. M. Three-dimensional flexible and conductive interconnected graphene networks grown by chemical vapour deposition. *Nat. Mater.* **2011**, *10*, 424–428.

[11] Kanoun, O.; Muller, C.; Benchirouf, A.; Sanli, A.; Dinh, T. N.; Al-Hamry, A.; Bu, L.; Gerlach, C.; Bouhamed, A. Flexible carbon nanotube films for high performance strain sensors. *Sensors* **2014**, *14*, 10042–10071.

[12] Amjadi, M.; Pichitpajongkit, A.; Lee, S.; Ryu, S.; Park, I. Highly stretchable and sensitive strain sensor based on silver nanowire–elastomer nanocomposite. *ACS Nano* **2014**, *8*, 5154–5163.

[13] Kim, Y.; Zhu, J.; Yeom, B.; Di Prima, M.; Su, X. L.; Kim, J. G.; Yoo, S. J.; Uher, C.; Kotov, N. A. Stretchable nanoparticle conductors with self-organized conductive pathways. *Nature* **2013**, *500*, 59–63.

[14] Kang, D.; Pikhitsa, P. V.; Choi, Y. W.; Lee, C.; Shin, S. S.; Piao, L. F.; Park, B.; Suh, K. Y.; Kim, T. I.; Choi, M. Ultrasensitive mechanical crack-based sensor inspired by the spider sensory system. *Nature* **2014**, *516*, 222–226.

[15] Yang, J.; Chen, J.; Su, Y. J.; Jing, Q. S.; Li, Z. L.; Yi, F.; Wen, X. N.; Wang, Z. N.; Wang, Z. L. Eardrum-inspired active sensors for self-powered cardiovascular system characterization and throat-attached anti-interference voice recognition. *Adv. Mater.* **2015**, *27*, 1316–1326.

[16] Wang, Y.; Yang, T. T.; Lao, J. C.; Zhang, R. J.; Zhang, Y. Y.; Zhu, M.; Li, X.; Zang, X. B.; Wang, K. L.; Yu, W. J. et al. Ultra-sensitive graphene strain sensor for sound signal acquisition and recognition. *Nano Res.* **2015**, *8*, 1627–1636.

[17] Zhao, W.; Luo, J.; Shan, S. Y.; Lombardi, J. P.; Xu, Y.; Cartwright, W.; Lu, S. S.; Poliks, M.; Zhong, C. J. Nanoparticle-structured highly sensitive and anisotropic gauge sensors. *Small* **2015**, *11*, 4509–4516.

[18] Stassi, S.; Cauda, V.; Canavese, G.; Pirri, C. F. Flexible tactile sensing based on piezoresistive composites: A review. *Sensors* **2014**, *14*, 5296–5332.

[19] Li, Z. T.; Wang, Z. L. Air/liquid-pressure and heartbeat-driven flexible fiber nanogenerators as a micro/nano-power source or diagnostic sensor. *Adv. Mater.* **2011**, *23*, 84–89.

[20] Pang, C.; Lee, G. Y.; Kim, T.; Kim, S. M.; Kim, H. N.; Ahn, S. H.; Suh, K. Y. A flexible and highly sensitive strain-gauge sensor using reversible interlocking of nanofibres. *Nat. Mater.* **2012**, *11*, 795–801.

[21] Nichols, W. W. Clinical measurement of arterial stiffness obtained from noninvasive pressure waveforms. *Am. J. Hypertens.* **2005**, *18*, 3S–10S.

[22] Lazović, B.; Mazić, S.; Zikich, D.; Žikić, D. The mathematical model of the radial artery blood pressure waveform through monitoring of the age-related changes. *Wave Motion* **2015**, *56*, 14–21.

[23] Simmons, J. G. Generalized formula for the electric tunnel effect between similar electrodes separated by a thin insulating film. *J. Appl. Phys.* **1963**, *34*, 1793–1803.

[24] Neugebauer, C. A.; Webb, M. B. Electrical conduction mechanism in ultrathin, evaporated metal films. *J. Appl. Phys.* **1962**, *33*, 74–82.

[25] Hu, N.; Karube, Y.; Yan, C.; Masuda, Z.; Fukunaga, H. Tunneling effect in a polymer/carbon nanotube nanocomposite strain sensor. *Acta Mater.* **2008**, *56*, 2929–2936.

[26] Tanner, J. L.; Mousadakos, D.; Giannakopoulos, K.; Skotadis, E.; Tsoukalas, D. High strain sensitivity controlled by the surface density of platinum nanoparticles. *Nanotechnology* **2012**, *23*, 285501.

[27] Farcau, C.; Moreira, H.; Viallet, B.; Grisolia, J.; Ciuculescu-Pradines, D.; Amiens, C.; Ressier, L. Monolayered wires of gold colloidal nanoparticles for high-sensitivity strain sensing. *J. Phys. Chem. C* **2011**, *115*, 14494–14499.

[28] Tian, H.; Shu, Y.; Wang, X. F.; Mohammad, M. A.; Bie, Z.; Xie, Q. Y.; Li, C.; Mi, W. T.; Yang, Y.; Ren, T. L. A graphene-based resistive pressure sensor with record-high sensitivity in a wide pressure range. *Sci. Rep.* **2015**, *5*, 8603.

[29] Chen, M. T.; Zhang, L.; Duan, S. S.; Jing, S. L.; Jiang, H.; Li, C. Z. Highly stretchable conductors integrated with a conductive carbon nanotube/graphene network and 3D porous poly(dimethylsiloxane). *Adv. Funct. Mater.* **2014**, *24*, 7548–7556.

[30] Segev-Bar, M.; Landman, A.; Nir-Shapira, M.; Shuster, G.; Haick, H. Tunable touch sensor and combined sensing platform: Toward nanoparticle-based electronic skin. *ACS Appl. Mater. Interfaces* **2013**, *5*, 5531−5541.

[31] Segev-Bar, M.; Konvalina, G.; Haick, H. High-resolution unpixelated smart patches with antiparallel thickness gradients of nanoparticles. *Adv. Mater.* **2015**, *27*, 1779–1784.

[32] Sun, P. Z.; Zhu, M.; Wang, K. L.; Zhong, M. L.; Wei, J. Q.; Wu, D. H.; Zhu, H. W. Small temperature coefficient of resistivity of graphene/graphene oxide hybrid membranes. *ACS Appl. Mater. Interfaces* **2013**, *5*, 9563−9571.